



UNIVERSITY POLITEHNICA of BUCHAREST

Doctoral School in Engineering and Applications of Lasers and  
Accelerators

Doctoral Thesis

**Simulation and design of the ELI-NP positron source  
and the slow positron beam pulsing system**

Doru Dinescu

Supervisor  
CS I Dr. Dimiter Balabanski

Author  
Doru Dinescu

Bucharest 2020



# Contents

<b>Contents .....</b>	<b>1</b>
<b>1. Introduction .....</b>	<b>3</b>
1.1. Fundamental properties of the positron and positronium .....	5
<b>2. Experimental methods with positrons. Positron Annihilation Spectroscopy .....</b>	<b>6</b>
2.1. Overview .....	6
2.2. Positron sources .....	6
2.3. Positron moderation .....	8
2.4. Charged particle transport in electromagnetic fields.....	9
2.5. Doppler Broadening Spectroscopy .....	9
2.6. Positron Annihilation Lifetime Spectroscopy .....	10
<b>3. The ELI-NP Positron Source - ELIPS. Positron beam formation and moderation.....</b>	<b>11</b>
3.1. The design of the positron spectroscopy laboratory at ELI-NP .....	11
3.2. The ELI-NP positron source. Beam formation. ....	13
3.3. Positron beam line optics. Focusing and guiding.....	14
3.4. Positron annihilation spectroscopy measurements for moderation materials. Experimental results.....	15
3.4.1. PAS on epitaxial GaN thin films .....	15
3.4.2. PAS on platinum foils .....	21
<b>4. The design and simulation of the pulsing system for the ELI-NP positron beam .....</b>	<b>25</b>
4.1. The design of the pulsing system. Beam bunching and chopping techniques .....	25
4.1.1. $e^+$ beam bunching .....	25
4.1.2. $e^+$ beam chopping .....	26
4.1.3. The design of the ELI-NP $e^+$ beam pulsing system.....	26
4.2. Simulations on the performance of the pulsing system. ....	27
4.2.1. Pre-buncher.....	27

1.1. Fundamental properties of the positron and positronium

4.2.2. Chopper .....	27
4.2.3. Main buncher.....	27
4.3. The design and simulation of the energy filter for backscattered positrons. ....	29
4.3.1. Simulation environments. Design of the setup.....	29
4.3.2. Simulation data analysis and results.....	30
<b>Conclusions and overview .....</b>	<b>33</b>
<b>Acknowledgments .....</b>	<b>35</b>
<b>References.....</b>	<b>36</b>

# Chapter 1

## 1. Introduction

Positron based techniques have proven over the years to be great tools for the study of the type and concentration of defects within new materials [1–3]. In the last decades there has been a push in solid state physics for the development of new materials with a wide range of applications [4]. Knowledge on the type and concentration of defects within new materials is of the utmost importance, as properties of interest may be affected (*i. e.* defects affect the mechanical properties of metals and ceramics, the conductivity in semiconductors, *etc.*), and a complete image on the physical properties may lead to new breakthroughs in the field.

Due to their positive charge positrons get trapped efficiently in places with low electron density within a material like open volume defects, vacancies, dislocations, *etc.* After their implantation positrons eventually annihilate with an electron of the material. The detection and the analysis of the annihilation radiation is the basis of Positron Annihilation Spectroscopy (PAS). The properties of the annihilation radiation depend on the electronic structure around the annihilation site. By measuring the positron lifetime from its implantation to its eventual annihilation within the material, information on the defect types and their relative concentration can be obtained. By measuring the broadness of the annihilation line, information on the electron momentum around the annihilation site can be acquired.

A comprehensive study on a studied material requires the use of complementary techniques, as there is no single method that can provide a complete image on all physical properties of interest. As the probe particle of PAS, the positron can penetrate a material over a distance ranging from few nanometres to few hundreds of nanometres, depending on its energy and on the material density. Since PAS studies are non-destructive, they represent a great tool to be used together with other techniques.

Conventional PAS methods use radioactive  $\beta^+$  emitters as positron sources. Since the positrons emitted by these kind of sources have a continuous energy spectrum with the highest energy generally up to hundreds keV, this permits the measurement only of bulk samples. Due to the constant developments in the field of modern advanced materials such as structured layered samples or thin films, advances have been made in the field of positron annihilation spectroscopy such that it can be

## 1.1. Fundamental properties of the positron and positronium

used to study almost any type of material. This has led to the creation of beams of monoenergetic positrons with variable energy. The mean positron implantation depth can be controlled from the surface to hundreds nanometres in depth by varying the positron energy, which allows for depth profiling of the studied sample.

A new slow positron beam line is under construction at the Extreme Light Infrastructure - Nuclear Physics (ELI-NP) facility in Romania. ELI-NP is one of the three pillars of the ELI project, which is a Pan-European effort aimed at becoming the world's first international laser research infrastructure [5]. ELI-NP is implemented to serve as a scientific research centre for nuclear physics experiments carried with the high intensity lasers ( $2 \times 10^{14}$  W) and \ or with the intense, high-brilliance  $\gamma$ -beam [6]. As part of the ELI-NP research program, the low energy arm of the  $\gamma$  beam system (up to 3.5 MeV) will be used for slow  $e^+$  production. The  $\gamma$ -beam will have an intensity of  $I_\gamma = 2.38 \times 10^{10} \gamma \text{ s}^{-1}$  and initially it was considered that it will be provided in macro bunches with a repetition rate of 100 Hz. Each macro bunch will consist of 32 micro bunches of  $\sim 1$  ps with 16 ns gap between each other [7]. Most of the work reported in this thesis refers to a  $\gamma$  beam which presents the previously described characteristics. The  $\gamma$  beam spot at the conversion point will have a diameter of 6.1 mm (FWHM). Simulations show that a slow  $e^+$  beam with an intensity of  $> 10^7 \text{ s}^{-1}$  can be obtained. In the first phase, the three spectrometers that will be available for positron studies are: Coincidence Doppler Broadening Spectroscopy (CDBS), Positron Annihilation Lifetime Spectroscopy (PALS) and Positron induced Auger Electron Spectroscopy (PAES). This thesis presents some particularities of the planned ELI-NP positron spectroscopy laboratory.

The first two chapters describe the basic concepts required to understand the principles of PAS. Firstly, information on the properties of the positron as well as its "fate" in matter is described. Chapter two focuses on the particularities of slow positron beams and touches topics like: positron sources, the creation of a monoenergetic slow positron beam, charged particle transport in a magnetic field, and details on some of the PAS methods.

The first part of the third chapter gives a brief overview on the planned ELI-NP positron spectroscopy laboratory. The second part of the chapter focuses on the PAS study of two kinds of moderation materials. Firstly, a study aimed at investigating the progress made in the fabrication of commercially available GaN epitaxial thin films as a possible material for field assisted  $e^+$  moderation, carried out by Doppler Broadening Spectroscopy (DBS), is presented. Secondly, the defect characterization by DBS and PALS of the Pt foils which will be used as a converter-moderator material at ELI-NP is given.

The fourth chapter gives information on the simulation and design of the pulsing system of the ELI-NP positron beam. The system is composed of a prebuncher, chopper, pre-accelerator, buncher, decelerator, accelerator, and bent drift tube. The first part of the chapter presents the simulated performances of each part of the system. The second part details the design and simulation of the energy filter for backscattered positrons.

## 1.1. Fundamental properties of the positron and positronium

Since the positron is the antiparticle of the electron, it has the same rest mass, rest energy and spin, but opposite electric charge (see Table 1.1).

**Table 1.1.** Properties of the positron [8].

<b>Rest mass</b>	$9.10938215(45) \cdot 10^{-31} \text{ kg}$
<b>Rest energy</b>	$0.510998910(13) \text{ MeV}/c^2$
<b>Charge</b>	$+ 1.602176487(40) \cdot 10^{-19} \text{ C}$
<b>Spin</b>	$1/2$

The result of positrons annihilating with an electrons is the emission of two or three  $\gamma$  quanta (or more  $\gamma$  quanta but with negligible branching ratio). The mode of annihilation is given by the spin state of the  $e^- - e^+$  pair.

Besides from annihilating, the electron and the positron can bind to form a hydrogen-like exotic atom called positronium (Ps). The mass of positronium equals twice the mass of the electron (1.022 MeV).

The singlet state,  $^1S_0$ , is known as para-positronium ( $p$ -Ps) and is characterized by antiparallel spins. In vacuum,  $p$ -Ps has a lifetime of 0.125 ns and decays predominantly by two  $\gamma$  quanta.

The triplet state,  $^3S_1$ , ortho-positronium ( $o$ -Ps), is characterized by parallel spins. In vacuum,  $o$ -Ps has a lifetime of  $\sim 142$  ns and decays predominantly by three  $\gamma$  quanta.

## Chapter 2

### 2. Experimental methods with positrons. Positron Annihilation Spectroscopy

#### 2.1. Overview

Positrons, due to their positive charge, are strongly repulsed from the positive ion cores and trapped inside negatively charged or neutral defects. When a positron is implanted in a material, it diffuses and eventually annihilates with an electron [1].

Conventional positron annihilation methods use energetic  $e^+$  directly emitted from radioisotopes such as  $^{22}\text{Na}$  and are suited to study bulk materials. For analysing subsurface layers and thin films, slow  $e^+$  beams are necessary. All PAS methods are based in the detection of the 511 keV  $\gamma$  quanta emitted after the positron annihilates with an electron. Because the positron is thermalized prior to the annihilation its kinetic energy is negligible when compared to the energy of the electrons in the solid. Thus variances in the properties of the annihilation radiation can only give information about the electron.

#### 2.2. Positron sources

##### Radioactive sources

Either for employing conventional PAS methods or in order to create monoenergetic slow positron beams most laboratories around the world use radioactive isotopes as the means to generate the particle of interest. Such sources consist of radioisotopes which are  $\beta^+$  emitters (see examples in Table 2.1).

**Table 2.1.** Properties of commonly used  $\beta^+$  - emitters. The data is taken from the *NuDat* database [9].

$\beta^+$ source	$T_{1/2}$	Intensity [%]	$E_{\text{average}}$ [keV]	$E_{\text{end}}$ [keV]
$^{22}\text{Na}$	2.6 years	89.84	215.5	545.5
$^{58}\text{Co}$	70.82 days	14.96	201.3	475.2
$^{64}\text{Cu}$	12.7 hours	17.86	278.1	652.5

The most suitable  $\beta^+$  source for positron production is the  $^{22}\text{Na}$  radioisotope. The decay scheme of  $^{22}\text{Na}$  is shown in Figure 2.1.

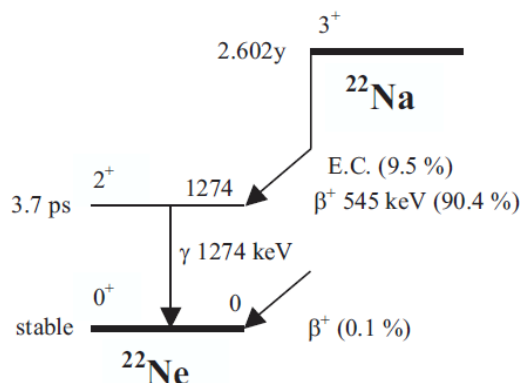


**Figure 2.1.** Decay scheme of  $^{22}\text{Na}$  [10]. This figure was adopted from ref. [11].

## Pair production

When a  $\gamma$  quantum enters a solid material, it interacts with a nucleus or an electron, and transfers its energy to the medium. By the interaction of  $\gamma$  photons with matter mainly three processes can occur: photoelectric effect, Compton scattering and pair production.

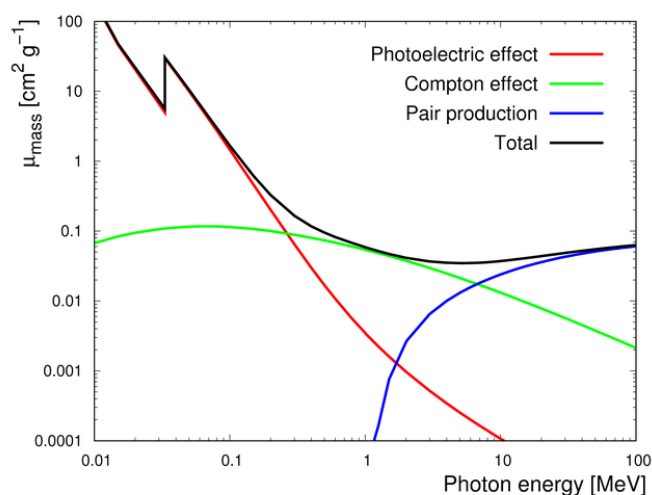


**Figure 2.2.** Variation of the mass attenuation coefficients for the photoelectric effect, Compton effect and pair production as a function of the photon energy. This figure was adopted from ref. [12]

When the energies of the  $\gamma$  photons surpass the threshold of at least the total rest mass energy of an electron positron pair (1.022 MeV), the pair production effect

## 2.3. Positron moderation

starts to appear. At the moment there are three main concepts implemented for creating positron beams through the mechanism of pair production. The first uses bremsstrahlung radiation from the highly energetic ( $\sim 10^1 - 10^2$  MeV) electrons coming from a LINAC to create electron – positron pairs in high Z materials. The other two methods are nuclear reactor based.

### 2.3. Positron moderation

All positrons coming from the sources mentioned in Chapter 2.2 are emitted with continuous spectral energies which cover a wide range. For the creation of monoenergetic slow positron beams there are two options. The first is to collimate the positron beam and to keep only those positrons within a narrow energy interval. The second method involves slowing down a large fraction of the positrons, such that most of them will end up with almost the same, low, energy. This process is usually performed through the interaction of a energetic positron beam with a solid material and it is called moderation.

Upon entering a solid, fast positrons rapidly lose their energy through inelastic collisions (see Figure 2.3).

The average distance travelled by a thermalized positron while diffusing in a material is called the diffusion length,  $L_+$ . If the target material has a negative positron work function the positrons which are thermalized within a subsurface layer of thickness of the order of  $L_+$  can be re-emitted into the vacuum.

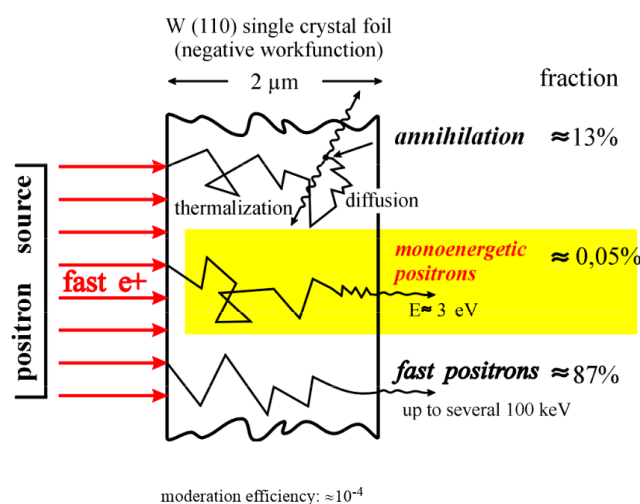


**Figure 2.3.** Processes that can take place when fast  $e^+$  enters in a solid. This figure was adopted from [13].

## 2.4. Charged particle transport in electromagnetic fields

The motion of a charged particle in a magnetic field is governed by the change in the direction of motion due to the presence of the electromagnetic field.

The equations of motion of a charged particle are described by:

$$\frac{d\mathbf{p}}{dt} = e \left[ \mathbf{E} + \frac{\mathbf{u}}{c} \times \mathbf{B} \right], \quad 2.1$$

$$\frac{dE}{dt} = e\mathbf{u} \cdot \mathbf{E}, \quad 2.2$$

for a particle with charge  $e$  which is moving in external fields,  $E$  and  $B$ .

Usually, this motion is described using the Lagrangian mechanics with generalized coordinates  $q_{i(t)}$  and  $\dot{q}_{i(t)}$ , in which the action,  $A$ , is described as the integral of  $\mathcal{L}$  between two periods of time,  $t_1$  and  $t_2$ :

$$A = \int_{t_1}^{t_2} \mathcal{L}[q_{i(t)}, \dot{q}_{i(t)}, t] dt. \quad 2.3$$

For a relativistic particle ( $\beta = v/c$ ) the Lagrangian,  $\mathcal{L}$ , takes the form:

$$\mathcal{L} = m_0 c^2 \left( 1 - \sqrt{1 - \beta^2} \right) + q(\vec{v} \cdot \vec{A} - \Phi), \quad 2.4$$

where  $\vec{A}$  is the magnetic vector potential,  $\Phi$  is the electric potential.

The motion of a charged particle in electromagnetic fields has been studied in great detail over the last decades, and detailed accounts regarding this subject can be found in many books (*i. e.* see ref. [14–16]).

## 2.5. Doppler Broadening Spectroscopy

As it can be seen in Figure 2.4, the momentum of the annihilating electron leads to deviations from the anti-collinearity and to a Doppler shift.

## 2.6. Positron Annihilation Lifetime Spectroscopy

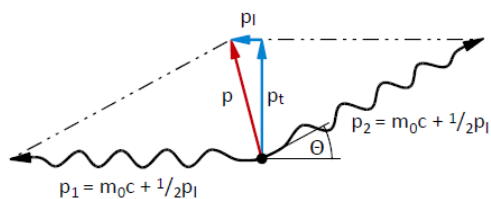


**Figure 2.4.** Deviation from the anti-collinearity and the Doppler shift of the annihilation quanta induced by the momentum of the annihilating electron. This figure was adopted from ref. [17].

The projection of longitudinal momentum component of the electrons leads to a Doppler shift which is detected as a broadening of the annihilation peak. Hence, the broadness is a measure for the energy distribution of the electrons involved in the annihilation process.

The background of such measurements can be reduced if a HPG detector is used in coincidence with another gamma ray detector to observe both annihilation gamma rays.

The coincidence curve is taken by detecting the two photons in coincidence whose energy satisfies the condition from Eq. 2.5

$$E_1 + E_2 = 2m_0c^2. \quad 2.5$$

## 2.6. Positron Annihilation Lifetime Spectroscopy

The cross section for the  $e^+$  annihilation within a material is described by:

$$\sigma = \frac{\pi_0^2 c}{v_{e^+}}, \quad 2.6$$

where  $v_{e^+}$  is the  $e^+$  velocity.

The  $e^+$  lifetime,  $\tau_{e^+}$ , can be derived from Eq. 2.6 as it follows:

$$\tau_{e^+} = \Gamma^{-1} = \frac{1}{\sigma v_{e^+} n_{e^-}} \propto \frac{1}{n_{e^-}}. \quad 2.7$$

From Eq. 2.7 it can be deduced that the  $e^+$  lifetime within a material is proportional to the density of electrons around the annihilation site,  $n_{e^-}$ , and in fact is inversely proportional to  $n_{e^-}$ . Because  $n_{e^-}$  around open volume defects is lower than the one in the perfect lattice, the  $e^+$  lifetime increases as they get trapped in defects.

PALS spectra consist of a sum exponential decaying components (Eq. 2.8), with positron being trapping in open-volume defects leading to long-lived components:

$$N(t) = \sum_{i=1}^n I_i \lambda_i \exp(-\lambda_i t), \quad 2.8$$

where  $n$  denotes the number of different states which positrons can annihilate from.

## Chapter 3

### 3. The ELI-NP Positron Source - ELIPS. Positron beam formation and moderation

#### 3.1. The design of the positron spectroscopy laboratory at ELI-NP

As part of the ELI-NP research program, the low energy  $\gamma$  beams will be used for slow  $e^+$  production. Thus, a new slow positron beam line, equipped at first with three spectroscopic systems, is being developed at ELI-NP. Figure 3.1. presents the layout of the ELI-NP positron spectroscopy laboratory.

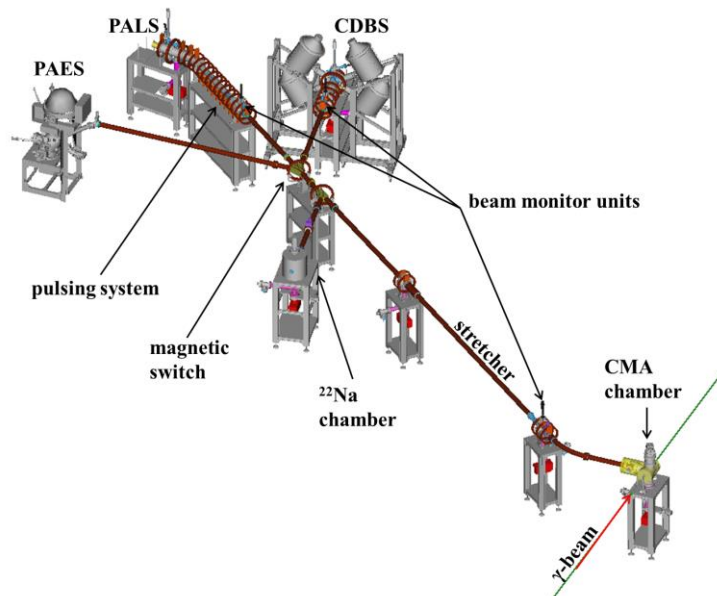


**Figure 3.1.** Layout of the ELI-NP positron spectroscopy laboratory.

Simulations show that a slow  $e^+$  beam with an intensity of  $\sim 2 \times 10^6 \text{ s}^{-1}$  can be achieved through conventional  $e^+$  moderation methods. The intensity of the  $e^+$  beam

### 3.1. The design of the positron spectroscopy laboratory at ELI-NP

can be increased to  $> 10^7 \text{ s}^{-1}$  if solid neon moderation is applied [18]. The slow  $e^+$  beam will be transported via magnetic fields to either of the three spectroscopic systems through vacuum lines equipped with solenoids and coils. In the first phase the three spectrometers that will be available are CDBS, PALS and PAES.

For year-round operation of the laboratory a radioactive  $^{22}\text{Na}$  source with an activity of maximum 50 mCi will also be used for slow  $e^+$  production [19].

#### CDBS

The design of the DBS \ CDBS spectrometer is presented in Figure 3.2. The detection system is comprised of 4 HPGe detectors.

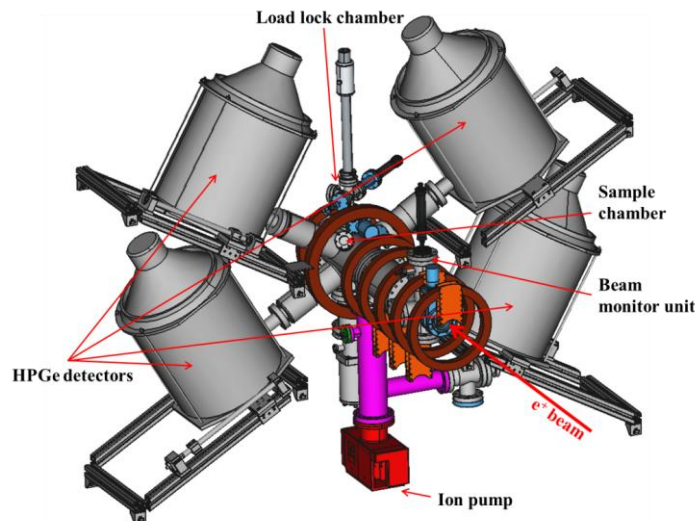


**Figure 3.2.** Design of the Coincidence Doppler Broadening Spectrometer

#### PALS

The design of the Positron Annihilation Lifetime Spectrometer is presented in Figure 3.3. The detection system consists of one scintillation detector placed behind the sample.

A pulsing system has been designed, so that the start signal is taken from the master clock of the chopper-buncher electronics of the pulsing system. The pulsing system is described in detail in Chapter 4.

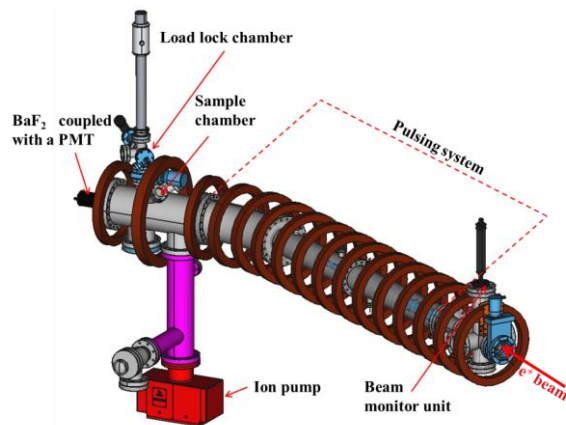


**Figure 3.3.** Design of the Positron Annihilation Lifetime Spectrometer

## PAES

The design of the Positron induced Auger Electron Spectrometer is presented in Figure 3.4. The system can perform Positron induced Auger Electron Spectroscopy, Electron induced Auger Electron Spectroscopy and X-ray Photoelectron Spectroscopy respectively.

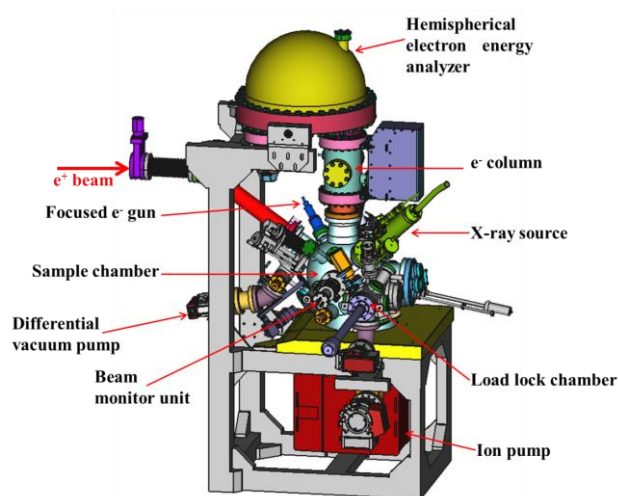


**Figure 3.4.** Design of the Positron induced Auger Electron Spectrometer, courtesy of SIGMA Surface Science™

## 3.2. The ELI-NP positron source. Beam formation.

The positron beam will be formed in the Converter Moderator Assembly (CMA) chamber (see Figure 3.1). The final source-CMA arrangement will work as presented in Figure 3.5.

### 3.3. Positron beam line optics. Focusing and guiding.

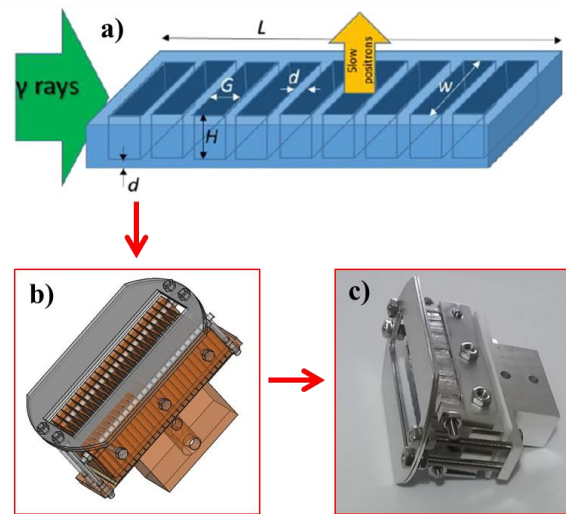


**Figure 3.5.** a) Venetian blind geometry of the proposed ELI-NP converter-moderator [18]; b) Design of the Converter Moderator Assembly; c) Manufactured Converter Moderator Assembly.

### 3.3. Positron beam line optics. Focusing and guiding.

After the moderation, the created slow  $e^+$ , are extracted in vacuum through a low electric field generated between the CMA and a highly transparent W mesh ( $> 95\%$  optical transmission). The focused beam enters the transport vacuum lines, which are equipped with solenoids and Helmholtz coils in order to create a guiding magnetic field.

The beam transport lines are equipped with three Beam Monitor Units (BMU) needed for a correct positioning of the slow  $e^+$  beam. The three BMUs are positioned at key locations along the transport lines (see Figure 3.1).

Based on the results presented in Chapter 3.1, 3.2 and 3.3, two articles were published in **Journal of Physics: Conference Series**, in the **Proceedings of the 14th International Workshop on Slow Positron Beam Techniques & Applications** (see ref. [20]) and in **Nuclear Instruments and Methods in Physics Research Section A: Accelerators, Spectrometers, Detectors and Associated Equipment** (see ref. [21]).

### 3.4. Positron annihilation spectroscopy measurements for moderation materials. Experimental results

#### 3.4.1. PAS on epitaxial GaN thin films

Due to the epithermal positron diffusion and the wide band gap of GaN (3.4 eV), the  $L_+$  value should be longer than the one in typical semiconductors. The expected long  $e^+$  diffusion length, the fact that GaN presents a negative  $e^+$  work function and the high breakdown voltage ( $\approx 1$  kV) suggests that GaN might be a suitable material for field assisted  $e^+$  moderation [22,23]. On the other hand,  $L_+$  reported in the literature for GaN are below 60 nm [24].

The aim of this study is to investigate by PAS the progresses made in the fabrication of commercially available GaN epitaxial thin films, grown on different substrates and with different thicknesses. The studied GaN thin films are produced by NTT Advanced Technology Corporation (Kanagawa, Japan) (ref. [25]). (see Table 3.1.)

**Table 3.1.** The name given to each sample set together with their respective GaN layer thickness and deposition substrate.

Sample name	GaN layer thickness (nm)	Substrate
GaN300/Si	300	Si
GaN700/Si	700	Si
GaN500/SiC	500	SiC
GaN300/Al <sub>2</sub> O <sub>3</sub>	300	Al <sub>2</sub> O <sub>3</sub>

#### Slow $e^+$ beam DBS measurements

The slow  $e^+$  beam measurements were carried out at the Institute of High Energy Physics of the Chinese Academy of Sciences with the system presented in Figure 3.6.

### 3.4. Positron annihilation spectroscopy measurements for moderation materials. Experimental results

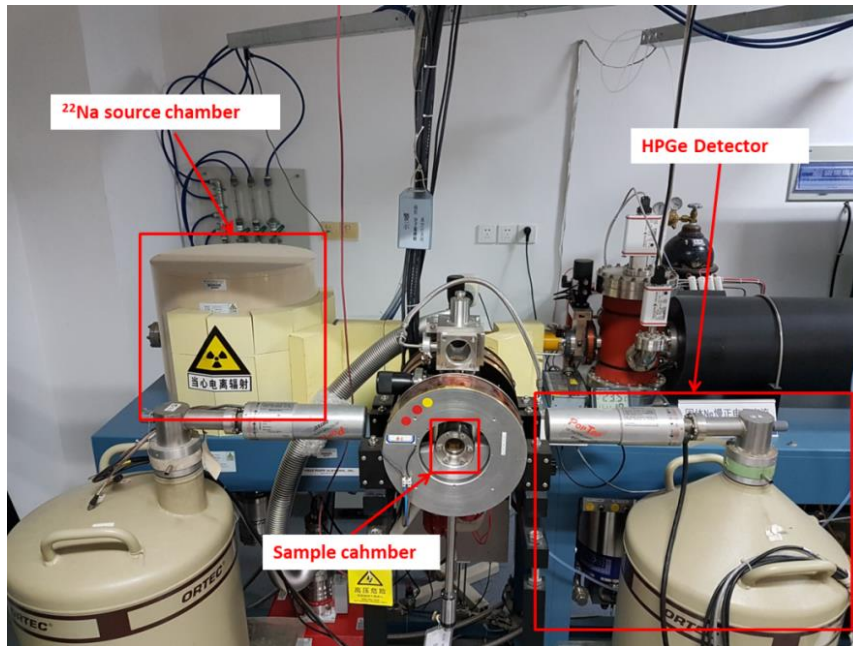


**Figure 3.6.** Slow  $e^+$  beam DB Spectrometer setup at the Institute of High Energy Physics of the Chinese Academy of Sciences

The VEPFIT software which solves the diffusion equation of the implanted positrons was used to fit the experimental data [26]. The positron transport equation is given by Eq. 3.1

$$D^+ \frac{d^2 c(z)}{dz^2} - \frac{d(v_d(z)c(z))}{dz} - k_t n_t(z)c(z) - \lambda_b c(z) + I_0 P(z, E_+) = 0, \quad 3.1$$

where  $D^+$  is the positron diffusion coefficient,  $v_d(z) = \mu(z)$  is the drift velocity of the positron with mobility  $\mu$  and electric field strength ( $z$ ),  $n_t(z)$  is the defect density,  $k_t$  is the rate constant of positrons being trapped at defects,  $\lambda_b$  is the bulk annihilation rate,  $I_0$  is the intensity of the implanted positrons [27].

The DBS measurements were performed by taking into account only the information supplied by the manufacturer for the samples. At a later stage upon analysing the structure of all samples by Transmission Electron Microscopy (TEM) at the Politechnica University of Bucharest, the existence of an aluminium nitrate, AlN, buffer layer was acknowledged for all the samples [28,29].

One of the parameters which is derived from the fit is the effective positron diffusion length ( $L_{\text{eff}}$ ) for each layer.  $L_{\text{eff}}$  is limited by the layer defects and is described by Eq. 3.2:

$$L_{\text{eff}} = \left[ \frac{D^+}{k_t n_t + \lambda_b} \right]^{1/2}, \quad 3.2$$

The depth profiles  $S(E_+)$  for the GaN300/Si and GaN700/Si are shown in Figure 3.7. The sharp initial decrease of  $S$  for  $E_+ \lesssim 1$  keV is due to annihilated epithermal positrons. At  $E_+ \gtrsim 1$  keV, it can be seen that  $S$  slowly increases with  $E_+$  in the GaN film range, while approaching the AlN buffer layer, a stronger increase starts (at  $E_+ \gtrsim 11$  keV) and tends to reach a saturation level in the Si substrate (better seen in Figure 3.7b). Based on the TEM information for the wafer layers, a three-layer (GaN, AlN, and Si) model was applied to fit the experimental  $S$  parameter by VEPFIT. The curves of the preliminary fits are very close to the fits showed in Figure 3.7. However, the best fit parameters revealed that the  $S_s \sim 0.445$  was found to be lower than  $S_{\text{GaN}} \sim 0.455$  (specific to positrons annihilated in GaN film). No Ps is formed in the bulk of GaN, however, at the surface, the branching ratio showed that 12% of the positrons form Ps [22].

Figure 3.8a and Figure 3.8b show the depth profiles  $S(E_+)$  for the GaN300/Al<sub>2</sub>O<sub>3</sub> and GaN500/SiC, respectively. For GaN300/Al<sub>2</sub>O<sub>3</sub> at  $E_+ \gtrsim 1$  keV a slower decrease of  $S$  with  $E_+$  is observed. (see Figure 3.8a). Since Ps is formed only at the GaN surface and not in the bulk [22] and the self-annihilation of its singlet form,  $p$ -Ps, contributes to the sharpening of the Doppler broadened annihilation line, the  $S_s$  is larger than  $S_{\text{GaN}}$  in the bulk of GaN film. This, along with the back-diffusion of thermalized positrons to the surface, explain the slow decrease. For the GaN500/SiC sample the behaviour of  $S$  with  $E_+$  follows the same pattern as for both GaN/Si samples and can be explained in an analogous way.

Saleh *et al.* suggested that the observed low  $L_{\text{eff}} < 60$  nm values of positron diffusion length in GaN are due to positron interaction with dislocations [24]. It should be mentioned that perfect lattice semiconductors are expected to have  $L_{\text{eff}}$  in the range 200–300 nm [30]. The longest effective positron diffusion length  $L_{\text{eff}} = 92 \pm 3$  nm for GaN was obtained for a hydride vapour phase epitaxy (HVPE) GaN [31]. The present study the best  $L_{\text{eff}}$  was obtained for the GaN500/SiC sample to be  $75 \pm 20$  nm.

### 3.4. Positron annihilation spectroscopy measurements for moderation materials. Experimental results

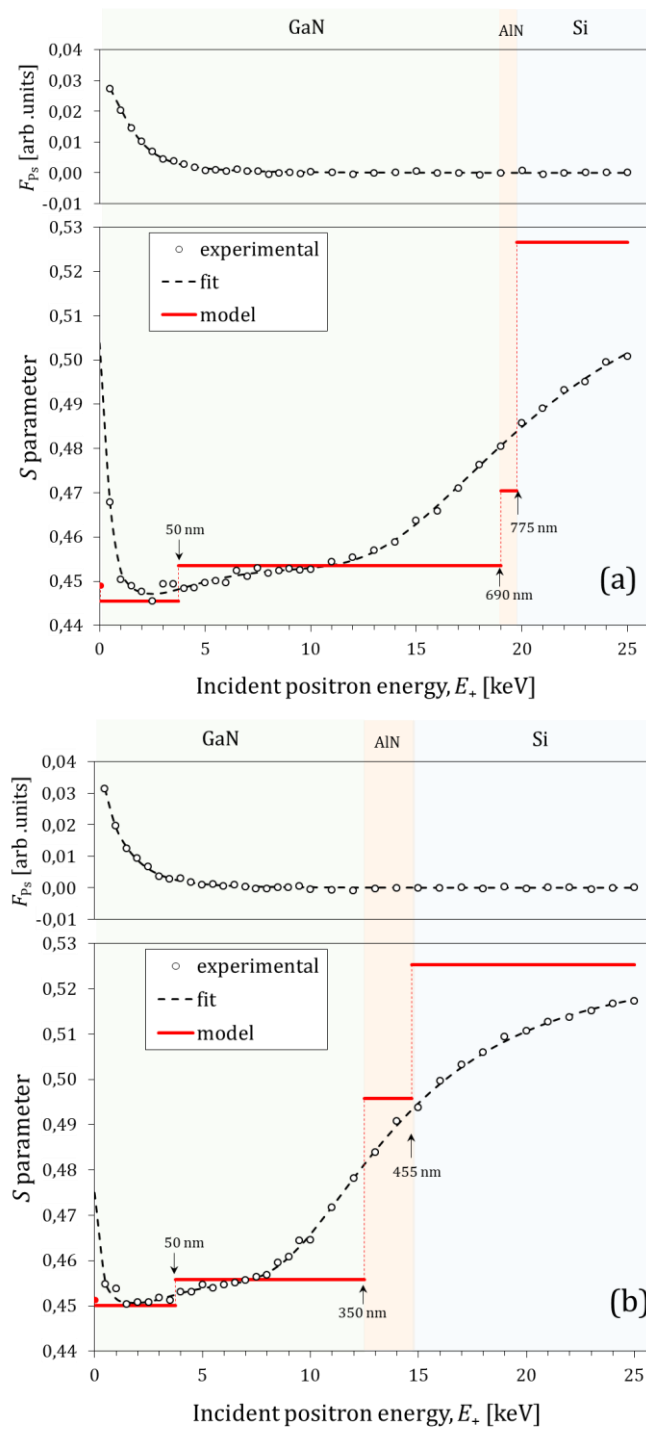


**Figure 3.7.** Plotted depth profiles  $S(E_+)$  of (a) GaN700/Si and (b) GaN300/Si. The experimental errors are in the order of the experimental point size. The stairs represent the best parameters obtained by the fit of a 4-layer model to the experimental data by the VEPFIT software. The upper part of figure is the experimental data and the best fit of the relative Ps fraction,  $F_{Ps}(E_+)$ .

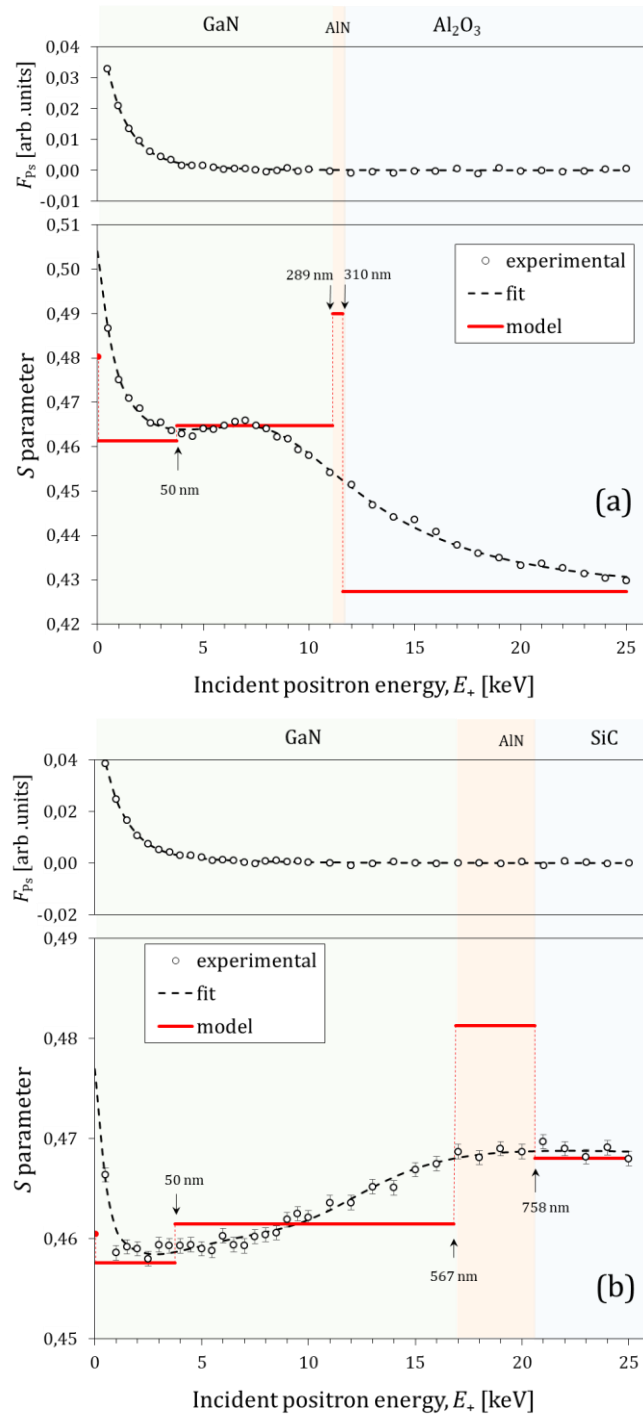


**Figure 3.8.** Plotted depth profiles  $S(E_+)$  of (a) GaN300/Al<sub>2</sub>O<sub>3</sub> and (b) GaN500/SiC. The experimental errors are in the order of the experimental point size. The stairs represent the best parameters obtained by the fit of a 4-layer model to the experimental data by the VEPFIT software. The upper part of figure is the experimental data and the best fit of the relative Ps fraction,  $F_{Ps}(E_+)$ .

3.4. Positron annihilation spectroscopy measurements for moderation materials. Experimental results

**Table 3.2.** Best fit parameters obtained by VEPFIT from the  $S(E_+)$  and  $F_{Ps}(E_+)$  depth profiles for the GaN300/Si sample. The values without error margins are fixed parameters.

Sample		GaN300/Si $\chi^2 = 1.15$		
Layer		$L_{\text{eff}}$ [nm]	$S$	$d$ [nm]
Sublayer				
GaN	GaN1	14.3 (5)	0.4501 (6)	50
	GaN2	22 (6)	0.4558 (4)	300
AlN		26 (10)	0.4957 (2)	105
Si		245	0.5254 (5)	-

**Table 3.3.** Best fit parameters obtained by VEPFIT from the  $S(E_+)$  and  $F_{Ps}(E_+)$  depth profiles for the GaN700/Si sample. The values without error margins are fixed parameters.

Sample		GaN700/Si $\chi^2 = 1.73$		
Layer		$L_{\text{eff}}$ [nm]	$S$	$d$ [nm]
Sublayer				
GaN	GaN1	13.1 (4)	0.4456 (4)	50
	GaN2	43 (6)	0.4536 (3)	640
AlN		4 (33)	0.4707 (3)	85
Si		245	0.5264 (1)	-

**Table 3.4.** Best fit parameters obtained by VEPFIT from the  $S(E_+)$  and  $F_{Ps}(E_+)$  depth profiles for the GaN300/Al<sub>2</sub>O<sub>3</sub> sample. The values without error margins are fixed parameters.

Sample		GaN300/Al <sub>2</sub> O <sub>3</sub> $\chi^2 = 1.39$		
Layer		$L_{\text{eff}}$ [nm]	$S$	$d$ [nm]
Sublayer				
GaN	GaN1	12.5 (4)	0.4613 (7)	50
	GaN2	41 (21)	0.4647 (4)	239
AlN		21 (4)	0.4901 (4)	21
Al <sub>2</sub> O <sub>3</sub>		80	0.4273 (3)	-

**Table 3.5.** Best fit parameters obtained by VEPFIT from the  $S(E_+)$  and  $F_{Ps}(E_+)$  depth profiles for the GaN300/SiC sample. The values without error margins are fixed parameters.

Sample		GaN500/SiC $\chi^2 = 1.18$		
Layer		$L_{\text{eff}}$ [nm]	$S$	$d$ [nm]
	Sublayer			
GaN	GaN1	13 (3)	0.4576 (4)	50
	GaN2	75 (20)	0.4615 (4)	517
AlN		25 (18)	0.4813 (2)	191
SiC		150	0.4680 (7)	-

Based on these results, two articles were published in *Nanomaterials* (Basel) (see ref. [28]) and *Materials* (Basel) (see ref. [29]). The articles were based on the collaborative work between two separate groups from ELI-NP, and one group from University Politehnica of Bucharest. From the published results only the Positron Annihilation Spectroscopy data was used in the present thesis.

### 3.4.2. PAS on platinum foils

A moderator's efficiency can be improved by increasing the probability of thermalized positrons to be re-emitted from the surface of the material. This probability is proportional to the  $e^+$  diffusion length,  $L_+$ , within the material. One of the ways of increasing  $L_+$  for metals such as W is to perform proper annealing. Tungsten needs annealing at temperatures of over 2000 °C in vacuum which is difficult as it would require a special type of oven. For this reason, and for the fact that tungsten is also difficult to machine to the required shape, it was decided that for the ELI-NP  $e^+$  source the convertor-moderator material of choice is Pt. Hugenschmidt *et al.* have already reported in ref. [32] that Pt yields similar results to W, in terms of  $\gamma$  to fast  $e^+$  conversion and  $e^+$  moderation.

The motivation behind the measurements was to determine the optimum annealing parameters of the Pt foils, through PAS methods. To achieve this, each set of 2 identical samples was annealed at different temperatures, and in different conditions (see Table 3.6).

### 3.4. Positron annihilation spectroscopy measurements for moderation materials. Experimental results

**Table 3.6.** The name given to each sample set together with their respective annealing temperature and duration, and atmospheric conditions

Sample name	Sample characteristics	Annealing temperature (°C)	Annealing conditions	Annealing duration (hours)
Pt600V1h		600	Vacuum ( $1 \times 10^{-5}$ mbar)	1
Pt1100A1h	2 Pt foils of $0.127 \times 10 \times 10$ mm	1100	Air ( $1 \times 10^3$ mbar)	1
Pt1100V1h		1100	Vacuum ( $1 \times 10^{-5}$ mbar)	1
Pt1100V4h		1100	Vacuum ( $1 \times 10^{-5}$ mbar)	4

### Conventional PALS measurements

Conventional PALS measurements were carried out at the Institute of High Energy Physics of the Chinese Academy of Sciences with the system presented in Figure 3.9.

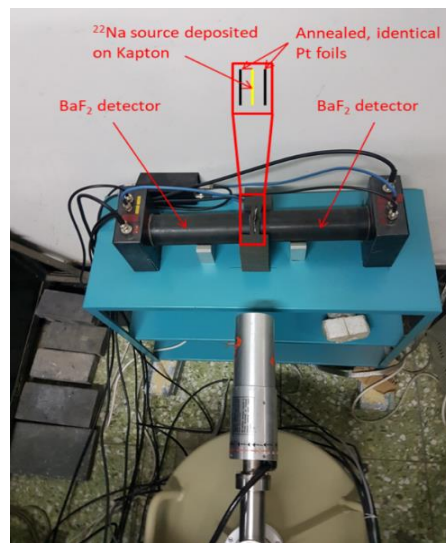


**Figure 3.9.** Conventional PAL Spectrometer setup at the Institute of High Energy Physics of the Chinese Academy of Sciences

The obtained lifetime spectra were analysed by LT9 software [33] in order to extract the positron lifetime in the studied material. As a result of the fitting of the lifetime spectra, the LT9 software [33] also calculates the mean lifetimes with their corresponding intensities.

The results obtained from the LT9 analysis of the measured spectra are presented in Table 3.7, together with theoretical and experimental data available in the literature for similar samples. It can be seen that for all the samples annealed at 1100 °C,  $\tau_1 = [104 - 108]$  ns which is close to the  $\tau_b$  of perfect lattice Pt, and is in good

agreement with the results reported in ref. [34] in which  $\tau_1$  was found to be 104 ps for a similar Pt foil annealed at 1600 K.

**Table 3.7.** Calculated mean lifetimes for each sample set, as obtained by the LT9 analysis together with theoretical and experimental data available in the literature.

Sample name	$\tau_1$ (ps)	$d\tau_1$ (ps)
Pt600V1h	132	2
Pt1100A1h	104	1
Pt1100V1h	104	1
Pt1100V4h	108	1
Pt (theoretical) [35]	99	-
Pt (experimental) [36]	110	3

### Slow $e^+$ beam DBS measurements

The slow  $e^+$  beam measurements were carried out in an analogous way to the DBS measurements presented in Chapter 3.4.1.

A more intuitive way of presenting the calculated  $S(E_+)$  and  $W(E_+)$  is to arrange them in an  $S$ - $W$  map. Figure 3.10 presents the  $S$ - $W$  map in which the points obtained experimentally are represented by the hollow markers. The best fit as obtained by the VEPFIT analysis of the  $S$  and  $W$  parameter was plotted as a trend line. In the figure there are also represented the characteristic  $S$  and  $W$  points for the bulk Pt annealed in each condition. It can be seen that the fitted lines follow the experimental points and that the calculated  $S$  and  $W$  parameters for each sample are placed on these fitted lines.

Table 3.8 presents the positron lifetime in the bulk as obtained by the LT9 analysis of the PALS data together with the calculated  $L_+$  and the best fit parameters obtained by the VEPFIT fitting of  $S(E_+)$  and  $W(E_+)$ . It can be observed that the results obtained by the Doppler broadening study by slow  $e^+$  beam confirm the results obtained by PALS.

### 3.4. Positron annihilation spectroscopy measurements for moderation materials. Experimental results

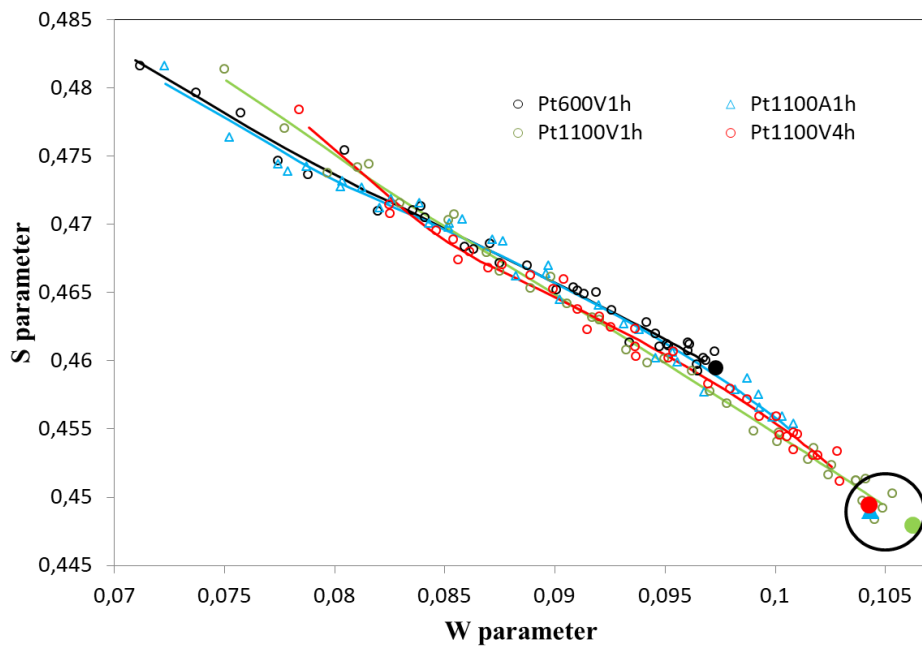


**Figure 3.10.** S-W map for all the annealed Pt foils (represented by the hollow markers) with the best fit VEPFIT obtained curves (represented by the trend lines) and the characteristic bulk S vs. W parameters as calculated by VEPFIT (represented by the larger filled markers)

**Table 3.8.** Positron lifetime in the bulk as obtained by the LT9 analysis of the PALS data. Best fit parameters obtained by the VEPFIT fitting of  $S(E_+)$  and  $W(E_+)$ .

Sample name	$\tau_1$ [ps]	$L_+$ [nm]	S	W
Pt600V1h	132 (2)	45 (2)	0.459 (2)	0.098 (1)
Pt1100A1h	104 (1)	173 (4)	0.449 (4)	0.104 (2)
Pt1100V1h	104 (1)	64 (1)	0.448 (2)	0.107 (2)
Pt1100V4h	108 (1)	114 (3)	0.449 (3)	0.104 (1)

The best  $L_+ = 173 \pm 4$  nm was obtained for the Pt1100A1h sample.

## Chapter 4

### 4. The design and simulation of the pulsing system for the ELI-NP positron beam

PALS is based on measuring the lifetime of a  $e^+$  within a solid. For PALS the stop signal is always taken from one of the two 511  $\gamma$  quanta emitted through the annihilation of the positron with an electron from the studied material. In order to perform PALS with a slow  $e^+$  beam a start signal is needed. Out of all the approaches to obtain a start signal for PALS with slow positron beams, the method with the best possible time resolution consists of injection of ultra-short pulses created by the chopping and bunching technique and using deriving the start signal from timing structure of the pulsing device.

#### 4.1. The design of the pulsing system. Beam bunching and chopping techniques

##### 4.1.1. $e^+$ beam bunching

For  $e^+$  beams the principle is based on adjusting longitudinal velocity of the positrons through a time dependent electric field. By doing so the positrons are either accelerated or decelerated, so their time of arrival at a certain place in space is controlled.

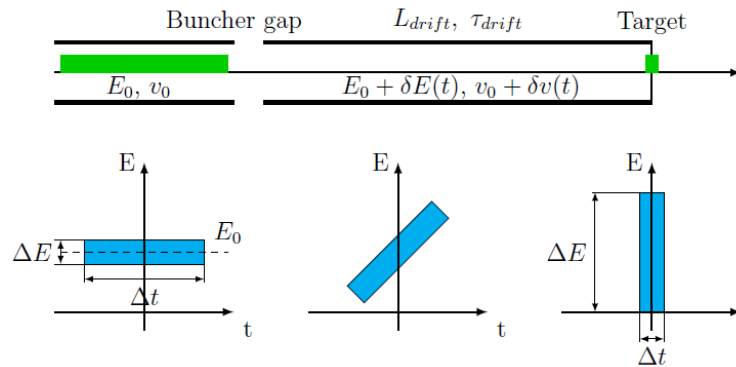


**Figure 4.1.** The working principle of a  $e^+$  beam buncher together with the phase – space transformation in accomplishes [37].  $E_0$  is the mean  $e^+$  beam energy and  $\Delta E$  is the energy spread. This figure was adopted from ref. [37].

Figure 4.1. presents working principle of a  $e^+$  beam buncher together with the phase – space transformation in accomplishes.

#### 4.1. The design of the pulsing system. Beam bunching and chopping techniques

##### 4.1.2. $e^+$ beam chopping

Beam chopping represents another method of producing a pulsed  $e^+$  beam from a continuous  $e^+$  source. For  $e^+$  beams, the construction of a chopper is usually accomplished by a beam deflector, or by the so-called retarding potential chopper type.

The retarding potential chopper type usually consists of three tungsten meshes of high ( $> 95\%$ ) optical transmission on which different potentials are applied. The first and last meshes are grounded, while on the central mesh a chopping signal is applied

##### 4.1.3. The design of the ELI-NP $e^+$ beam pulsing system

The designed pulsing system is presented in Figure 4.2.

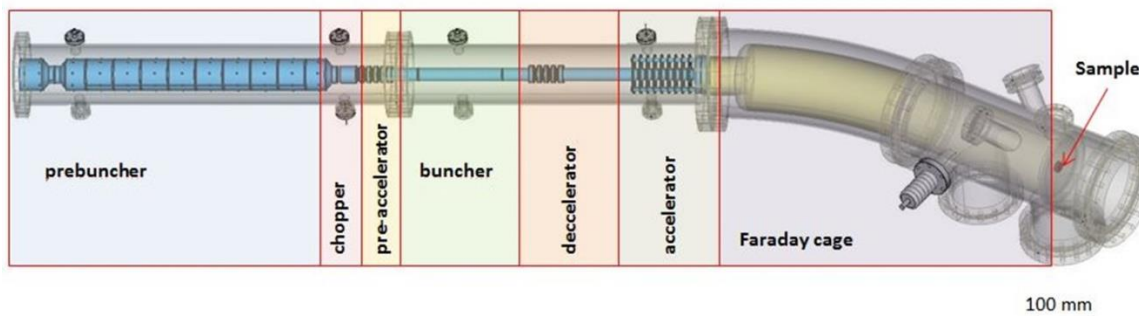


**Figure 4.2.** The 3D design of the in vacuum electrodes of the pulsing system. It consists of a prebuncher, chopper, pre-accelerator, buncher, decelerator, accelerator, and drift bent tube.

A Matlab™ program [38] was developed to calculate the movement of positrons in time varying electric fields. The system was designed for incoming continuous or Direct Current (DC) beam of positrons with energy of 29 eV with a realistic energy distribution of 1 eV (FWHM).

## 4.2. Simulations on the performance of the pulsing system.

### 4.2.1. Pre-buncher

The purpose of a pre-buncher is to bunch the positrons in such a way that when the chopping interval is applied to the beam, losses in the beam intensity are minimised.

For the simulation, a sawtooth wave of 40 MHz  $\sim t^2$  with an amplitude of 8 V was used. The resulting time compression after the DC  $e^+$  beam passed the pre-buncher is shown in Figure 4.3.

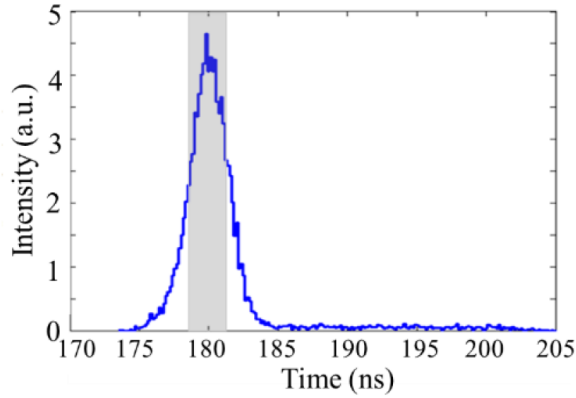


**Figure 4.3.** The simulated time compression of  $e^+$  after the pre-buncher.

### 4.2.2. Chopper

The purpose of a chopper is to filter out those positrons which will not arrive at the proper time at the buncher gaps. As a result, the chopping eliminates possible satellite peaks in the spectrum and improves the peak to background ratio. The time compression achieved by the pre-buncher and the width of the chopper transmission window determines the beam intensity losses due to the pulsing system. For the signals described above the transmission efficiency of the pulsing system is 65%.

### 4.2.3. Main buncher

The main buncher is the second time focusing component of the pulsing system. In order to minimize the chromatic aberration in this component (due to the

#### 4.2. Simulations on the performance of the pulsing system.

energy modulation introduced by the pre-buncher as the first focusing component), after the chopper, the positrons are pre-accelerated to 1.5 keV [39].

The designed main buncher is a simple single frequency (120 MHz) sine-wave double gap buncher with a 96 mm central electrode. The effect of the buncher on the phase space of the positrons is shown in Figure 4.4.

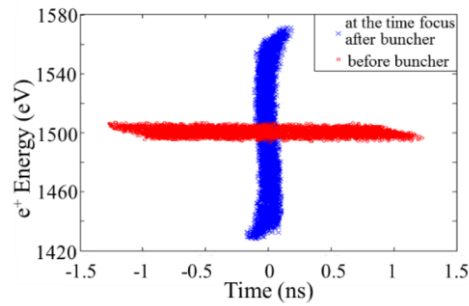


**Figure 4.4.** The phase space of the positrons before the buncher (in red) and at the target position (in blue).

The resulted time distribution of the  $e^+$  in a pulse is very close to a Gaussian with FWHM = 109 ps (see Figure 4.5).

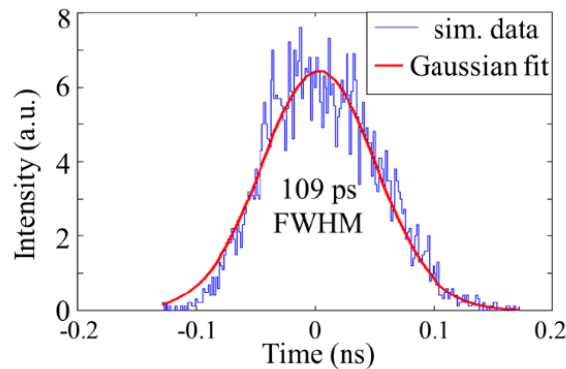


**Figure 4.5.** The time distribution of 1.5-keV  $e^+$  at the target position. The data are fitted well by a Gaussian with FWHM=109 ps.

**Based on the results presented in Chapter 4.2, an article was published in Journal of Physics: Conference Series, in the Proceedings of the 14th International Workshop on Slow Positron Beam Techniques & Applications (see ref. [40]).**

### 4.3. The design and simulation of the energy filter for backscattered positrons.

When incident positrons hit the target a fraction of them is backscattered. If the backscattered positrons reach back the accelerator they can be reflected by the electric field and implanted into the sample with a delay from the initial  $e^+$  bunch. This causes significant distortions in the PALS spectrum as satellite peaks [41–43]. As it can be seen in Figure 4.2, at ELI-NP a bent tube equipped with steering coils, is foreseen to be implemented in the designed pulsing system to minimise distortions in the PLS spectra.

#### 4.3.1. Simulation environments. Design of the setup.

Comsol Multiphysics<sup>®</sup> [44] was used for simulating the magnetic field that will guide the  $e^+$  beam from the accelerator to the centre of the sample, and for the generation of the electric field of the accelerator (see Figure 4.6).

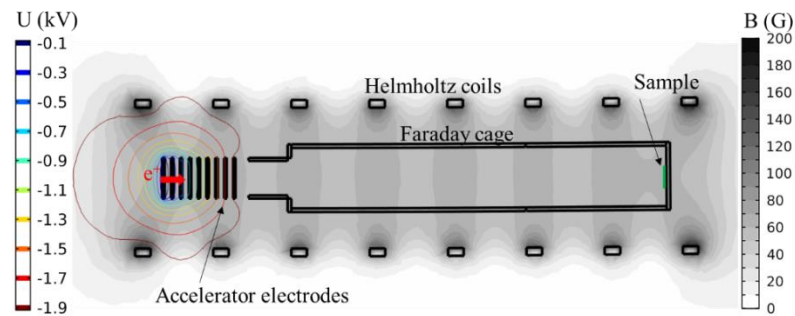


**Figure 4.6.** The cross section of the 3D maps along the central beam line axis represented by a surface plot of the magnetic field and contour lines of the electric field in the case of a straight tube and potential  $U_{acc} = -2$  kV.

The 3D maps of the Comsol simulations were exported into an ASCII format in which the values of the magnetic and electric fields were taken point by point in a grid pattern, and imported into the Geant4 software where the simulations regarding  $e^+$  backscattering were performed.

The physics models in Geant4 do not account for the  $e^+$  lifetime in a material, therefore the time histogram actually does not represent a PALS spectrum but only the resolution function,  $R(t)$ . If positrons annihilate from a discrete number of states, the PALS spectrum can be described as a convolution of the resolution function and the probabilities to decay from those states:

### 4.3. The design and simulation of the energy filter for backscattered positrons.

$$y(t) = R(t) \otimes (N_t \sum_{i=1}^n \left(\frac{I_i}{\tau_i}\right) \exp\left(-\frac{t}{\tau_i}\right) + B), \quad 4.1$$

In order to study the effect of backscattered positrons, we simulated PALS spectra convoluting the resolution function  $R(t)$  with four components with lifetimes  $[\tau_1, \tau_2, \tau_3, \tau_4] = [0.1, 0.5, 3, 20]$  ns and corresponding intensities  $[I_1, I_2, I_3, I_4] = [10, 60, 10, 20]\%$ .

Example of a simulated spectrum is shown in Figure 4.7a. Figure 4.7b presents a simulated spectrum with suppressed backscattering for comparison.

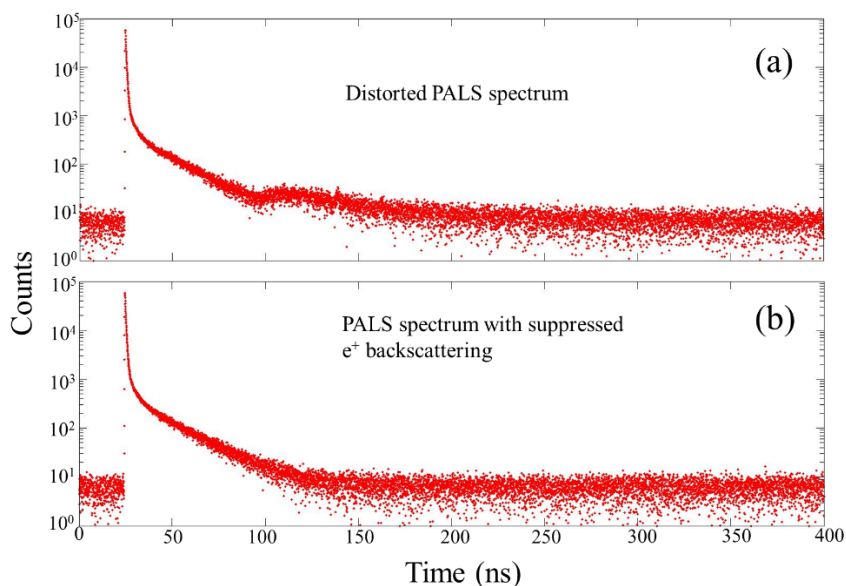


**Figure 4.7.** Simulated PALS spectra for a beam of  $E_+ = 2$  keV in a straight tube geometry. b) Simulated PALS spectra for a beam of  $E_+ = 2$  keV in a straight tube geometry with suppressed  $e^+$  backscattering.

#### 4.3.2. Simulation data analysis and results.

For minimizing the effect of  $e^+$  backscattering, two possible solutions were simulated. Both solutions can be seen in Figure 4.8. The first solution is to add an aperture at the accelerator exit with a diameter,  $D$ , comparable with the beam spot size. The second solution is to pass the accelerated  $e^+$  beam through a bent tube equipped with steering coils to act as a velocity filter.

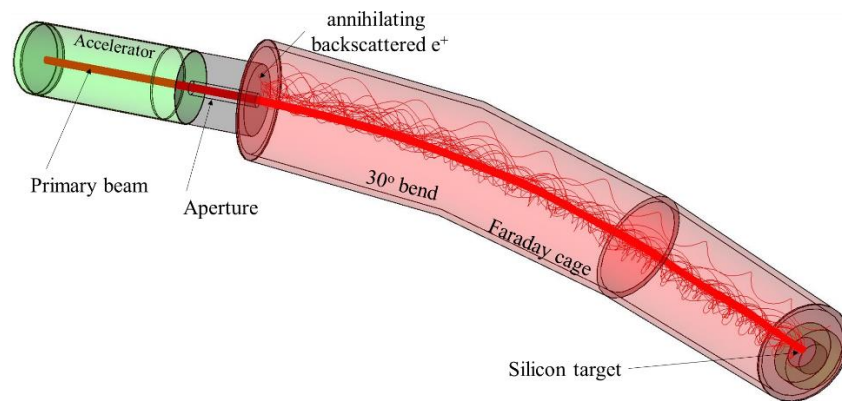


**Figure 4.8.** The trajectories of a 2 keV  $e^+$  beam and the event of  $e^+$  backscattering with 1000 incident particles. Example of a  $30^\circ$  bend with an aperture of  $D = 15$  mm obtained by Geant4.

Figure 4.9. presents simulated PALS spectra for a beam of  $E_+ = 5$  keV in a straight tube geometry with two different aperture sizes (60 and 15 mm).

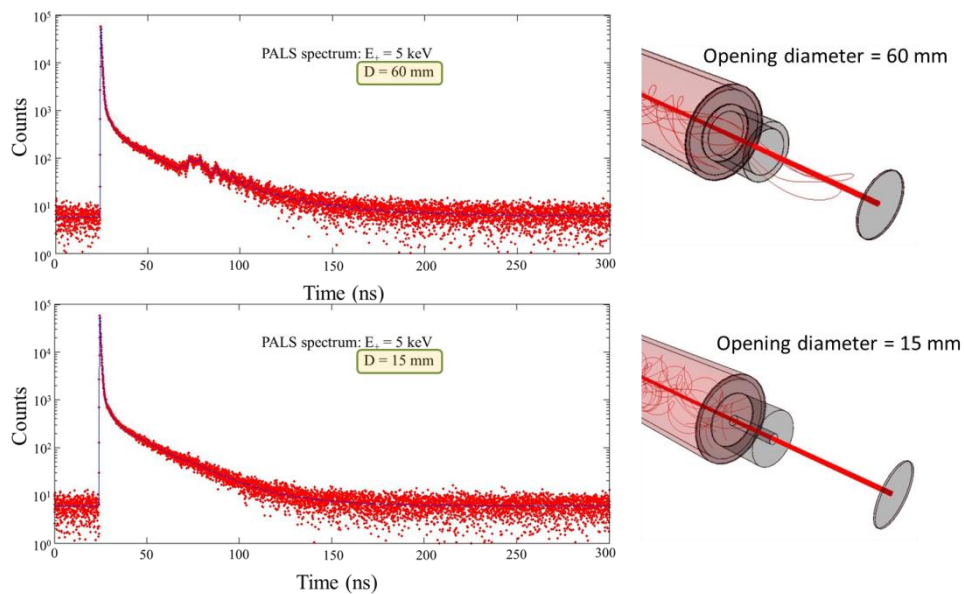


**Figure 4.9.** Simulated PALS spectra for a beam of  $E_+ = 5$  keV in a straight tube geometry with two different aperture sizes.

By applying the second solution, meaning to pass the accelerated  $e^+$  beam through a bent tube equipped with steering coils to act as a velocity filter, will force the backscattered  $e^+$  beam to steer away from the aperture opening. This effect can be visualised in Figure 4.10.

#### 4.3. The design and simulation of the energy filter for backscattered positrons.

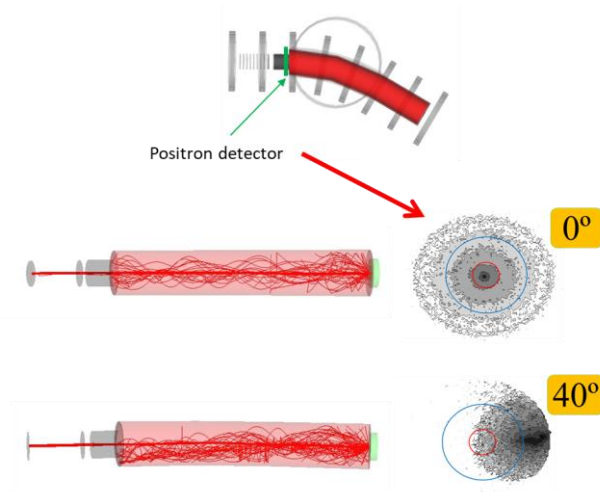


**Figure 4.10.** Backscattered  $e^+$  beam deviation away from the aperture opening, with the angle of the bend. The red circle represents a 15 mm aperture opening, while the blue one represents a 60 mm aperture opening.

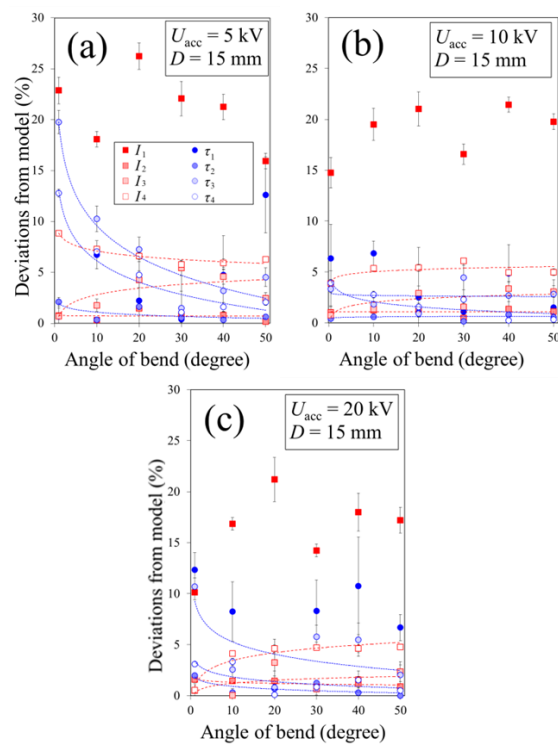


**Figure 4.11.** Fit parameter deviations from the model PALS spectra for a  $e^+$  beam of different energies: a)  $E_+ = 5$  keV, b)  $E_+ = 10$  keV and c)  $E_+ = 20$  keV as a function of the bend angle.

The performed Geant4 simulations have helped to identify the origin of the distortions in the PALS spectra caused by  $e^+$  backscattering. The simulations have

shown that adding an aperture at the accelerator exit in combination with bending a part of the Faraday cage, which acts as a velocity filter, is a satisfactory solution to reduce the distortions. The obtained results show that for bend angles  $\geq 30^\circ$  the deviation from the model parameters induced by the  $e^+$  backscattering starts to saturate, reaching  $\Delta_i < 5\%$  for  $E_+$  in the interval 2 - 20 keV.

**Based on the results presented in Chapter 4.3, two articles were published in Acta Physica Polonica Series A (see ref. [45]) and in U.P.B. Scientific Bulletin, Series A (see ref. [46]).**

## Conclusions and overview

This thesis presented the general plans for the ELI-NP positron spectroscopy laboratory together with a detailed account of two particularities. A PAS experiment was carried out at the Institute of High Energy Physics of the Chinese Academy of Sciences, Beijing, for the characterization of one type of field assisted moderator material, GaN thin films, by DBS, while the latter method, together with PALS were employed in order to determine the optimum annealing parameters for the ELI-NP material of choice for the  $\gamma$  to  $e^+$  conversion and fast  $e^+$  moderation. The second particularity of the ELI-NP laboratory, which is described in detail in this thesis, is the conceptual design of the pulsing system for the PALS experiment. Details on the design and simulation on the performance of the pulsing system are presented in detail in Chapter 4.

In the present study out of all four GaN samples the best effective positron diffusion length was obtained for the 500 nm thick GaN film grown on a SiC substrate, to be  $75 \pm 20$  nm. The studied materials, because of their high amounts of edge and screw dislocations, diffusion and partial non-stoichiometry, still imply several limitations in their use in the field of positron moderation.

The second PAS study was carried with the goal of determining the best possible annealing parameters for the ELI-NP converter-moderator material. The study was necessary because for the application of slow  $e^+$  beams it is of great importance to maximize the moderator's efficiency. The best positron diffusion

#### 4.3. The design and simulation of the energy filter for backscattered positrons.

length,  $L_+ = 173 \pm 4$  nm, was obtained for the sample annealed at 1100 °C in air for 1 hour.

The second part of the thesis presented in detail the positron beam pulsing system developed for the implementation of the PALS experiment. The ELI-NP pulsing system will be composed of a prebuncher, chopper, pre-accelerator, buncher, decelerator, accelerator, and bent drift tube. The designed system combines the most recent developments made in the field of charged particle beam pulsing in order to obtain the best possible positron pulse time compression at the target position. Firstly, simulations on the performance of the pulsing system are presented. The optimized MATLAB simulations have proven that the time distribution of the positrons in a pulse at the target position is very close to a Gaussian with FWHM = 109 ps. In the second part of Chapter 4 a detailed account on the design and simulation of the energy filter for backscattered positrons is presented. Such an energy filter is necessary in order to minimize distortions in the PALS spectra caused by backscattered positrons. The solution which will be implemented at ELI-NP consists in a bent tube, equipped with steering coils which acts as an energy filter. The obtained results show that for bend angles  $\geq 30^\circ$  the deviation from the model parameters induced by the  $e^+$  backscattering starts to saturate, reaching  $\Delta_i < 5\%$  for  $E_+$  in the interval 2 –20 keV. The  $30^\circ$  bend can be considered as an optimal solution which should be sufficient to minimize the effect of the backscattered positrons.

Nowadays in Europe there are only two user based positron spectroscopy facilities, both located in Germany, a successful implementation of the presented positron spectroscopy laboratory will prove beneficial for the scientific community, as there is a growing interest in the study of advanced materials. Furthermore, with the implementation of a new Variable Energy Gamma-ray (VEGA) system at ELI-NP, the  $\gamma$  beam will be provided with high spectral density ( $\geq 500$  photons/s/eV) in macro bunches with a repetition rate of 40 MHz [47]. The only part of the positron spectroscopy laboratory that is changed by the new VEGA system is that there is no need for a  $e^+$  pulse stretcher, as the positron beam will be created as quasi continuous due to the high repetition rate of the  $\gamma$  beam. The rest of the parameters of the ELI-NP positron beam presented in this thesis will remain unchanged.

## Acknowledgments

First and foremost I would like to thank my coordinator, Dr. Nikolay Djourellov, without whom this thesis would not have existed. He introduced me to the field of positron annihilation spectroscopy, and over the years developed my interest in the subject. I would like to thank him for his understanding and calm, even in cases when these were not warranted, and for patiently transferring his knowledge in the field to me.

I would like to thank my supervisor, Prof. Dimiter Balabanski, for giving me the opportunity to be part of the ELI-NP positron spectroscopy laboratory, which allowed me to carry my PhD studies. I would like to thank him for the many advices and for the constant encouragement, which allowed me to develop as a research scientist. Also, I have to thank Dr. Victor Leca, as he is the one which suggested that I join the ELI-NP team, and Prof. Calin Ur for giving me the opportunity to be part of the S.D.I.A.L.A PhD program.

I want to express my gratitude to the positron spectroscopy group at the Institute of High Energy Physics of the Chinese Academy of Sciences, especially to Dr. Wang Bao-Yi and Dr. Cao Xing-Zhong for allowing me to carry the positron annihilation studies necessary for this thesis in their laboratory.

Last but not least I would like to thank all the members of the Gamma Driven Experiments Department and of the Technical Division of ELI-NP, as completing this thesis would not be possible if not for the right colleagues, and a great work environment.

The work reported in this thesis was supported by the project Extreme Light Infrastructure Nuclear Physics (ELI-NP) Phases I and II, a project co-financed by the Romanian Government and European Union through the European Regional Development Fund.

## References

- [1] P. G. Coleman, *Positron Beams and Their Applications* (World Scientific Publishing Co. Pte. Ltd., Singapore, 2000).
- [2] R. Krause-Rehberg and H. S. Leipner, *Positron Annihilation in Semiconductors: Defect Studies* (Springer-Verlag, Berlin Heidelberg, 1999).
- [3] Y. C. Jean, P. E. Mallon, and D. M. Schrader, *PRINCIPLES AND APPLICATIONS OF POSITRON AND POSITRONIUM CHEMISTRY* (World Scientific Publishing Co. Pte. Ltd., Singapore, 2003).
- [4] S.-H. Chang, I. A. Parinov, and V. Yu. Topolov, *Advanced Materials: Physics, Mechanics and Applications* (Springer International Publishing Switzerland, 2014).
- [5] <https://Eli-Laser.Eu/the-Eli-Project/> (n.d.).
- [6] S. Gales, K. A. Tanaka, D. L. Balabanski, et al., *Reports on Progress in Physics* **81**, 094301 (2018).
- [7] O. Adriani and et al., *ArXiv.Org Accelerator Physics (physics.acc-ph)*, **arXiv:1407.3669**, (2014).
- [8] P. J. Mohr, D. B. Newell, and B. N. Taylor, *Journal of Physical and Chemical Reference Data* **45**, 043102 (2016).
- [9] [http://NuclearData.Nuclear.Lu.Se/ Database/NuDat/](http://NuclearData.Nuclear.Lu.Se/Database/NuDat/). (n.d.).
- [10] <https://Nds.Iaea.Org/Relnsd/Vcharhtml/VChartHTML.html> (n.d.).
- [11] I. Procházka, *Materials Structure* **8**, (2001).
- [12] <https://Www.Fe.Infn.It/Radioactivity/Educational/Detection.html> (n.d.).
- [13] R. Krause-Rehberg, [http://Positron.Physik.Uni-Halle.de/Talks/ICPA-15\\_ISPS\\_lecture\\_RKR.Pdf](http://Positron.Physik.Uni-Halle.de/Talks/ICPA-15_ISPS_lecture_RKR.Pdf) (n.d.).
- [14] J. D. Jackson, *Classical Electrodynamics, 3rd Edition* (John Wiley & Sons, Inc, New York, 1999).
- [15] In *Electromagnetism* (John Wiley & Sons, Ltd, 2013), pp. 443–465.
- [16] N. Anderson, *The Electromagnetic Field* (Springer, Boston, MA, 1968).
- [17] C. Piochacz, PhD Thesis (2009).
- [18] N. Djourelou, C. Hugenschmidt, S. Balascuta, et al., *Romanian Reports in Physics* **68**, 735 (2016).
- [19] I. Dobrin, N. Djourelou, D. Enache, et al., *UPB Scientific Bulletin, Series A: Applied Mathematics and Physics* **81**, 241 (2019).

- [20] N. Djourellov, A. Oprisa, D. Dinescu, et al., *Journal of Physics: Conference Series* **791**, 012011 (2017).
- [21] N. Djourellov, D. Dinescu, and V. Leca, *Nuclear Instruments and Methods in Physics Research Section A: Accelerators, Spectrometers, Detectors and Associated Equipment* **934**, 19 (2019).
- [22] L. V. Jørgensen and H. Schut, *Applied Surface Science* **255**, 231 (2008).
- [23] J. P. Merrison, M. Charlton, B. I. Deutch, et al., *Journal of Physics Condensed Matter* **4**, L207 (1992).
- [24] Sagr Saleh, and Awla Moftah Elhasi, *American Journal of Modern Physics* **3**, 24 (2014).
- [25] <https://www.Ntt-at.Com/> (n.d.).
- [26] A. van Veen, H. Schut, J. de Vries, et al., in *American Institute of Physics Conference Series* (1991), pp. 171–198.
- [27] A. van Veen, H. Schut, M. Clement, J. de Nies, A. Kruseman, M. Ijpma, *Appl. Surf. Sci.* **85**, 216 (1995).
- [28] V. L. Ene, D. Dinescu, N. Djourellov, et al., *Nanomaterials (Basel)* **10**, (2020).
- [29] V. L. Ene, D. Dinescu, I. Zai, et al., *Materials (Basel)* **12**, (2019).
- [30] P. J. Schultz, E. Tandberg, K. G. Lynn, et al., *Phys. Rev. Lett.* **61**, 187 (1988).
- [31] A. Uedono, M. Malinverni, D. Martin, et al., *Journal of Applied Physics* **119**, 245702 (2016).
- [32] C. Hugenschmidt, G. Kögel, R. Repper, et al., *Nuclear Instruments and Methods in Physics Research Section B: Beam Interactions with Materials and Atoms* **198**, 220 (2002).
- [33] J. Kansy, *Nuclear Instruments and Methods in Physics Research Section A: Accelerators, Spectrometers, Detectors and Associated Equipment* **374**, 235 (1996).
- [34] G. Brauer, W. Anwand, E.-M. Nicht, et al., *Phys. Rev. B* **62**, (2000).
- [35] J M Campillo Robles, E Ogando and F Plazaola, *J. Phys.: Condens. Matter* **19**, (2007).
- [36] J. M. C. Robles, F Plazaola, *Trans Tech Publications Defect and Diffusion Forum Vols*, 213 (2003).
- [37] L. Ravelli, PhD Thesis (2014).
- [38] MATLAB, *Version R2010a* (The MathWorks Inc., Natick, Massachusetts, 2010).
- [39] A. Laakso, PhD Thesis (2005).
- [40] N. Djourellov and D. Dinescu, *Journal of Physics: Conference Series* **791**, 012010 (2017).

- [41] M. Jungmann, J. Haerberle, R. Krause-Rehberg, et al., *Journal of Physics: Conference Series* **443**, 012088 (2013).
- [42] H. Marinov, N. Djourelov, P. Nedelec, et al., *Nuclear Instruments and Methods in Physics Research A* **729**, 569 (2013).
- [43] P. Willutzki, J. Stormer, G. Kogel, et al., *Measurement Science and Technology* **5**, 548 (1994).
- [44] COMSOL Multiphysics®, [Www.Comsol.Com](http://www.comsol.com), Stockholm, Sweden (n.d.).
- [45] D. Dinescu and N. Djourelov, *Acta Physica Polonica A* **132**, 1624 (2017).
- [46] D. Dinescu and N. Djourelov, *U.P.B. Sci. Bull., Series A* **79**, 317 (2017).
- [47] [Www.Eli-Np.Ro](http://www.eli-np.ro) (n.d.).